Weierstrass Function Methodology for Uncertainty Analysis of Random Media Criticality with Spectrum Range Control

Taro Ueki[a]*

[a]*Nuclear Safety Research Center, Japan Atomic Energy Agency, Ibaraki-Ken, Japan*

*Corresponding author

Email address: ueki.taro@jaea.go.jp

Physical address: 2-4 Ooaza Shirakata, Tokai-Mura, Naka-Gun, Ibaraki-Ken, Japan

319-1195

Accepted manuscript for https://doi.org/10.1016/j.pnucene.2021.104099

Weierstrass Function Methodology for Uncertainty Analysis of Random Media Criticality with Spectrum Range Control

Randomized Weierstrass function (RWF) has been under development for evaluating the uncertainty of random media criticality due to the material mixture in disorder. In this work, the modelling capability of RWF is refined so that the spectrum range can be controlled by specifying its lower and upper ends of the frequency domain variable. As a result, it becomes possible to make fair criticality comparison among replicas of random media under inverse power law power spectra. Technically, the infinite sum of trigonometric terms in RWF is formally extended to cover the arbitrarily low frequency domain and then truncated to finite terms for the sole purpose of spectrum range control. This means that the refined RWF is free of the issue of convergence towards a reference fractal characteristic of Weierstrass function and thus termed Incomplete Randomized Weierstrass function (IRWF). As a demonstration, a three-dimensional version of IRWF is applied to the mixture of three fuels with different burnups in a sufficiently water-moderated environment. Monte Carlo criticality calculations are carried out to evaluate the uncertainty of neutron effective multiplication factor (k_{eff}) due to the indeterminacy of mixture formation.

Keywords: Weierstrass function; random media; power spectrum; inverse power law; Monte Carlo criticality calculation

1. Introduction

In quite a general perspective, the dynamical system under extreme physical disorder has the tendency of evolving toward the equilibrium state characterized by an inverse power law power spectrum (Frieden and Huges, 1994). For example, fractional Brownian motion (FBM) (Reed et al, 1995) and Kolmogorov law of turbulence (Tatsumi, 1982) exhibit such a power spectrum and there are many phenomena in different fields under the same type of power spectrum (Bak et al, 1987; Dalziel et al, 1999; Miller et al, 1993). In reality, extreme physical disorder can indeed occur in high energy density devices if

engineering control is completely lost. Here, the loss of control under high energy density is one of the characteristics of a severe nuclear accident which undergoes the formation of a molten fissile substance of unknown nature called fuel debris. Its composition will eventually be revealed at points of measurements. However, it is very difficult, though not impossible, to estimate the spatial distribution of the composition of fuel debris. To cope with this issue, RWF (Ueki 2017, Ueki 2021) was developed as a randomized form of Weierstrass function for modelling the indeterminacy of fuel debris formation. The priority of RWF was placed on the mixture of constituent materials by way of molten transitional states with no intervention of control as opposed to the stochastic tessellation approach geared toward material fragmentation (Lamier et al, 2018; Marinosci et al, 2018).

The main topic in this paper is a practically-implementable representation of the macroscopic cross section of a material mixture formed via extreme disorder. Here, the material mixture is typically represented by the spatial distribution of volume fractions of constituent materials; extreme disorder, if left intact, eventually leads to the state characterized by the inverse power law power spectrum (Frieden and Huges, 1994) as mentioned earlier. In order to bring these points into action, it is important to start an investigation from representing a variation in space whose power spectrum is governed by the inverse power law power spectrum in terms of wave number (unit: 1/length). To this end, an ideal process is FBM since its power spectrum is exactly under the inverse power law over the whole domain of wave numbers (Reed et al, 1995). However, the integration of inverse power from zero to infinity diverges while the integration of a power spectrum observed in or constructed from measurements is usually finite. Faced with such a conflict between modelling and reality, it is worthwhile investigating a function which possesses some of the many reference characteristics of FBM. The fractal

dimension is one of the reference characteristics of complex systems and Weierstrass function is known to possess the same fractal dimension as FBM (Falconer, 2003). Moreover, both of FBM and Weierstrass function are continuous and non-differentiable everywhere (Falconer, 2003). Based on these common natures, RWF was utilized for generating random media replicas consisting of fuel and concrete and evaluating the uncertainty of criticality due to the indeterminacy of mixture formation (Ueki, 2017). It was also shown that the power spectrum of RWF is a discrete representation of the inverse power law power spectrum (Ueki, 2021). In this respect, RWF appears to give reactor physicists an analysis option for evaluating the criticality of fuel debris in terms of various inverse power law power spectra. However, RWF has no capability of specifying the upper and lower ends of a frequency domain variable. The control capability of spectral range should be built into RWF so that one could carry out the engineering uncertainty analysis of random media criticality under a fair and unified condition.

The main body of this paper consists of three sections. In Section 2, after a very brief review of RWF, the infinite sum of trigonometric terms in RWF is formally extended to cover the arbitrarily low spectrum range and then truncated to finite terms. It is shown that the discrete representation of any inverse power law power spectrum is obtained along with an arbitrarily set spectrum range. Since the truncation is not introduced in terms of keeping as many terms as practically possible for preserving the fractal nature of Weierstrass function, the resulting randomized function is termed IRWF with I indicating “incomplete”. In Section 3, numerical results are demonstrated for the criticality of fuel mixture in a sufficiently water-moderated environment by utilizing IRWF and partial volume pairing (PVP) (Ueki, 2021). The fluctuation of k_{eff} is shown under fair conditions of spectrum range which cannot be set for RWF (Ueki 2017, Ueki

2021; Araki et al, 2021). All the developments have been implemented in the Monte Carlo solver Solomon (Nagaya et al, 2019). Conclusions are summarized in Section 4.

2. IRWF

RWF is a randomized function defined as

$$W(x) = \sigma\sum_{j=1}^{\infty} B_j \lambda^{-\alpha j} \sin\left(\lambda^j x + A_j\right), \sigma > 0, \lambda > 1, 0 < \alpha < 1, \quad (1)$$

where σ is a constant for amplitude adjustment, B_j are independent random variables with zero mean and unit variance, and A_j are independent random variables uniformly distributed on $[0,2\pi)$. The independent variable x is multiplied by the power of a real number λ larger than unity unlike the Fourier series while the inverse power of λ is multiplied for ensuring convergence. The original deterministic form of Eq (1) is Weierstrass function

$$\sigma\sum_{j=1}^{\infty} \lambda^{-\alpha j} \sin\left(\lambda^j x\right) \quad (2)$$

which has the same fractal dimension $2 - \alpha$ as that of FBM with index α (Falconer, 2003). RWF in Eq (1) can be extended to

$$W(x) = \sigma\sum_{j=-M}^{\infty} B_j \lambda^{-\alpha j} \sin\left(\lambda^j x + A_j\right), \quad (3)$$

where M is an arbitrarily large fixed integer. As will be shown later, the power spectrum of Eq (3) ranges over $[\varepsilon, \infty)$ where ε is an arbitrarily small positive number. Now, for the purpose of spectral range control, terms with large and small summation indices are truncated to obtain

$$W(x) = \sigma\sum_{j=m1}^{\mathrm{m2}} B_j \lambda^{-\alpha j} \sin\left(\lambda^j x + A_j\right),$$

$$\lambda > 1, \alpha \geq 0, -\infty < m1 < m2 < \infty, \quad (4)$$

where $m1$ can be any integer because of the setup of M in Eq (3). In previous works (Ueki, 2017; Ueki, 2021), under the restriction of $0 < \alpha < 1$ as in Eq (1), $m2$ was taken to be as large as practically possible in order to maintain a characteristic of the fractal dimension

$2-\alpha$ shared by Weierstrass function and FBM. On the other hand, the index α in Eq (4) can be any non-negative values. More importantly, the truncation of terms at $j = m2$ makes a complete break with the preservation of fractal nature in the limit of $m2 \to \infty$ since, as will be shown later, the upper end of summation indices is determined for the sole purpose of specifying the highest end of the spectral range. Because of this breakup with fractal, $W(x)$ in Eq (4) is termed IRWF as referred to in Section 1.

Concerning the power spectrum of IRWF, one can resort to the Wiener-Khinchin theorem by way of the following steps. Firstly, the use of the properties of A_j and B_j yields

$$E[W(x)] = 0, \tag{5}$$

$$E[(W(x))^2] = \frac{\sigma^2}{2}\sum_{j=m1}^{m2} \lambda^{-2\alpha j}, \tag{6}$$

$$\begin{aligned} &E[(W(x+u) - W(x))^2] \\ &= 4\sigma^2 E[\sum_{j=m1}^{m2} \left(\lambda^{-\alpha j} \cos\left(\lambda^j \left(x + \frac{u}{2}\right) + A_j\right) \sin\left(\lambda^j \frac{u}{2}\right)\right)^2] \\ &= 2\sigma^2 \sum_{j=m1}^{m2} \lambda^{-2\alpha j} \sin^2(\lambda^j \frac{u}{2}), \end{aligned} \tag{7}$$

where $E[\cdot]$ stands for expectation. Secondly, Eqs (6)-(7) lead to

$$E[W(x)W(x+u)] = \frac{\sigma^2}{2}\sum_{j=m1}^{m2} \lambda^{-2\alpha j} \cos(\lambda^j u). \tag{8}$$

Since Eqs (5) and (8) do not depend on x, IRWF is stationary. Finally, according to the Wiener-Khinchin theorem, the Fourier transform of Eq (8) with respect to u yields the power spectrum of $W(x)$:

$$\begin{aligned} P(k;W) &= \int_{-\infty}^{\infty} E[W(x)W(x+u)] e^{-iku} du \\ &= \frac{\sigma^2}{4}\sum_{j=m1}^{m2} \lambda^{-2\alpha j} \int_{-\infty}^{\infty} \left(\exp\left(i\left(\lambda^j - k\right)u\right) + \exp\left(-i\left(\lambda^j + k\right)u\right)\right) du, \end{aligned} \tag{9}$$

where k is wave number. Using the infinite plane wave representation of Dirac delta function

$$\delta(y) = \frac{1}{2\pi}\int_{-\infty}^{\infty} e^{iyu}\, du \tag{10}$$

(a brief sketch of proof is found in [8]), Eq (9) is rewritten as

$$P(k;W) = \frac{\pi\sigma^2}{2}\sum_{j=m1}^{m2} \lambda^{-2\alpha j}\left[\delta\left(k-\lambda^j\right)+\delta\left(k+\lambda^j\right)\right] \tag{11}$$

For $\alpha > 0$, the integration of Eq (11) over $\left[\lambda^{m1-1}, \lambda^j\right]$ is

$$\int_{\lambda^{m1-1}}^{\lambda^j} P(k;W)dk = \int_{\lambda^{m1}}^{\lambda^j} P(k;W)dk = \frac{\pi\sigma^2}{2}\sum_{i=m1}^{j} \lambda^{-2\alpha i}$$

$$= \frac{\pi\sigma^2 \lambda^{2\alpha(1-m1)}}{2\left(\lambda^{2\alpha}-1\right)}\left(1-\frac{\lambda^{2\alpha(m1-1)}}{\lambda^{2\alpha j}}\right), m1 \le j \le m2 \tag{12}$$

while the integration of $1/k^{2\alpha+1}$ over the same range yields

$$\int_{\lambda^{m1-1}}^{\lambda^j} \frac{dk}{k^{2\alpha+1}} = \frac{\lambda^{2\alpha(1-m1)}}{2\alpha}\left(1-\frac{\lambda^{2\alpha(m1-1)}}{\lambda^{2\alpha j}}\right), m1 \le j \le m2. \tag{13}$$

The dependency on $k = \lambda^j$ in Eq (12) is the same as that in Eq (13), which means that IRWF in Eq (4) is a discrete representation of the inverse power law power spectrum $1/k^{2\alpha+1}$ for $\alpha > 0$ and covers the spectrum over $\left[\lambda^{m1-1}, \lambda^{m2}\right]$. Similarly, the power spectra of Eqs (1) and (3) range over $[1, \infty)$ and $[\varepsilon, \infty)$, respectively, where ε is a positive value λ^{-M-1} which is arbitrarily close to zero. Obviously, RWF in Eq (1) utterly lacks the control capability of spectral range.

For $\alpha = 0$, the integration of Eq (11) over $\left[\lambda^{m1-1}, \lambda^j\right]$ is

$$\int_{\lambda^{m1-1}}^{\lambda^j} P(k;W)dk = \int_{\lambda^{m1}}^{\lambda^j} P(k;W)dk = \frac{\pi\sigma^2}{2}(j-m1+1)$$

$$= \frac{\pi\sigma^2}{2\ln(\lambda)}\ln\left(\frac{\lambda^j}{\lambda^{m1-1}}\right), m1 \le j \le m2 \tag{14}$$

while the integration of $1/k$ over the same range yields

$$\int_{\lambda^{m1-1}}^{\lambda^j} \frac{dk}{k} = \ln\left(\frac{\lambda^j}{\lambda^{m1-1}}\right), m1 \le j \le m2. \tag{15}$$

The dependency on $k = \lambda^j$ in Eq (14) is the same as that in Eq (15), which means that IRWF in Eq (4) with $\alpha = 0$ is a discrete representation of the exact inverse power law power spectrum $1/k$.

Typical use of Eq (11) is as follows. Suppose that one wants to express the spectral range $0.1 \leq k \leq 100$ with 45 teeth (representation points). In this case, by setting $\lambda^{m2} = 100$, $\lambda^{m2-m1+1} = 100/0.1 = 1000$ and $m2 - m1 + 1 = 45$, one obtains $m1 = -14$, $m2 = 30$ and $\lambda = 1.166$. On the other hand, in previous works on RWF (Ueki, 2017; Ueki, 2021), $m2$ was taken as the smallest integer M' satisfying $\lambda^{-\alpha M'} < 0.01$ for $\alpha > 0$ while λ was always fixed to 1.5, which implies no capability of specifying the highest end of spectral range. In addition, since $\alpha = 0$ was forbidden due to the convergence issue in Eq (1), the RWF for the $1/k$ spectrum representation required $M' > 1000$ as in a setting of $\alpha = 0.01$, $\lambda = 1.5$ and $\lambda^{-1136\alpha} = 0.00999$. The spectrum range $k < 1$ was utterly excluded in RWF because of the fixed setting of $m1 = 1$. All these limitations and unpractical aspects are overcome in IRWF.

In order to search for the power spectrum $1/k^{2\alpha+1}$ for $\alpha < 0$ that cannot be realized by Eq (4), IRWF is also proposed as

$$Y(x) = \sigma \sum_{j=m1}^{m2} B_j \lambda^{\alpha j} \sin\left(\lambda^{-j} x + A_j\right),$$

$$\lambda > 1, \alpha < 0, -\infty < m1 < m2 < \infty. \tag{16}$$

Here, the exponents in $\lambda^{\alpha j}$ and λ^{-j} have the same sign unlike the exponents of λ in Eq (4). By way of the same steps as in the derivation of Eq (8), one obtains from Eq (16)

$$E[Y(x)Y(x+u)] = \frac{\sigma^2}{2} \sum_{j=m1}^{m2} \lambda^{2\alpha j} \cos\left(\lambda^{-j} u\right). \tag{17}$$

Taking into account $E[Y(x)] = 0$ and using the Wiener Khinchin theorem with Eq (10), Eq (17) yields

$$P(k;W) = \frac{\pi\sigma^2}{2} \sum_{j=m1}^{m2} \lambda^{2\alpha j} \left[\delta\left(k - \lambda^{-j}\right) + \delta\left(k + \lambda^{-j}\right)\right]. \tag{18}$$

Here, the integration of Eq (18) over $\left[\lambda^{-j}, \lambda^{-(m1-1)}\right]$ is

$$\int_{\lambda^{-j}}^{\lambda^{-(m1-1)}} P(k;W)dk = \int_{\lambda^{-j}}^{\lambda^{-m1}} P(k;W)dk = \frac{\pi\sigma^2}{2} \sum_{i=m1}^{j} \lambda^{2\alpha i}$$

$$= \frac{\pi\sigma^2\lambda^{2\alpha m1}}{2(1-\lambda^{2\alpha})}\left(1-\frac{\lambda^{2\alpha(1-m1)}}{\lambda^{-2\alpha j}}\right), m1 \le j \le m2 \quad (19)$$

while the integration of $1/k^{2\alpha+1}$ over the same range yields

$$\int_{\lambda^{-j}}^{\lambda^{-(m1-1)}} \frac{dk}{k^{2\alpha+1}} = \frac{\lambda^{2\alpha(m1-1)}}{2(-\alpha)}\left(1-\frac{\lambda^{2\alpha(1-m1)}}{\lambda^{-2\alpha j}}\right), m1 \le j \le m2. \quad (20)$$

The dependency on $k = \lambda^{-j}$ in Eq (19) is the same as that of Eq (20), which means that IRWF in Eq (16) is a discrete representation of the power law power spectrum $1/k^{2\alpha+1}$ for $\alpha < 0$ and covers the spectrum over $\left[\lambda^{-m2}, \lambda^{-(m1-1)}\right]$.

Typical use of Eq (18) is as follows. Suppose that one wants to express the spectral range $0.1 \le k \le 100$ with 45 teeth (representation points). Then, by setting $\lambda^{-m2} = 0.1$, $\lambda^{m2-m1+1} = 100/0.1 = 1000$ and $m2 - m1 + 1 = 45$, one obtains $m1 = -29$, $m2 = 15$ and $\lambda = 1.166$. In previous work (Ueki, 2021), $k > 1$ and $k < 1$ were excluded for $\alpha < 0$ and $\alpha > 0$, respectively, by the fixed setting of $m1=1$. It was thus impossible to make fare comparison for the spectra $1/k^{\beta}$, $0<\beta<1$ and $1/k^{\beta}$, $1<\beta<2$. This limitation is overcome in a pair of IRWFs in Eqs (4) and (16). Overall, the conditions $m1 = 1$ with $\lambda^{-\alpha m2} < 0.01$ for $\alpha > 0$ and $\lambda^{\alpha m2} < 0.01$ for $\alpha < 0$ in line with the convergence of Weierstrass function in Eq (2) has been lifted so that the spectral range can be realized in a desired range.

Three-dimensional versions of IRWF are

$$W(\mathbf{r}) = \sigma\sum_{j=m1}^{m2} B_j\lambda^{-\alpha j}\sin\left(\lambda^j \mathbf{r}\bullet\boldsymbol{\Omega}_j/S + A_j\right),$$

$$\lambda > 1, \alpha \ge 0, -\infty < m1 < m2 < \infty, \quad (21)$$

$$Y(\mathbf{r}) = \sigma\sum_{j=m1}^{m2} B_j\lambda^{\alpha j}\sin\left(\lambda^{-j} \mathbf{r}\bullet\boldsymbol{\Omega}_j/S + A_j\right),$$

$$\lambda > 1, \alpha \le 0, -\infty < m1 < m2 < \infty, \quad (22)$$

where $\mathbf{r}$ is a vector in three-dimensional Euclidean space, $\boldsymbol{\Omega}_j$ independent vectors uniformly distributed over the unit sphere, and S a scaling factor which is introduced as

a scale of spatial variation independent of spectral characteristics (Ueki, 2017). When $\alpha = 0,\ j = m1, \ldots, m2$ in Eq (21) and $j = -m2, \ldots, -m1$ in Eq (22) yield $W(\mathbf{r}) = Y(\mathbf{r})$. For $\alpha > 0$, Eq (21) is bounded by

$$|W(\mathbf{r})| \leq \sigma \frac{\lambda^{-\alpha(m1)}(1-\lambda^{-\alpha(m2+1-m1)})}{1-\lambda^{-\alpha}} \tag{23}$$

if B_j are chosen as the independent Bernoulli random variables taking ±1 equally likely. When applied to the fluctuation of volume fractions, $|W(r)| \leq 1$ is required. In this case, σ is chosen to be

$$\sigma \leq \frac{\lambda^{\alpha(m1)}(1-\lambda^{-\alpha})}{1-\lambda^{-\alpha(m2+1-m1)}},\ \alpha > 0. \tag{24}$$

For the same reasoning,

$$\sigma \leq \frac{1}{m2+1-m1},\ \alpha = 0, \tag{25}$$

$$\sigma \leq \frac{\lambda^{-\alpha(m1)}(1-\lambda^{\alpha})}{1-\lambda^{\alpha(m2+1-m1)}},\ \alpha < 0. \tag{26}$$

Figure 1 displays replicas of IRWF for α=0.5, 0 where σ is determined by the equalities in Eqs (24) and (25). The left subfigure corresponds to the power spectrum of $1/k^2$ (α=0.5) and the fractal nature of Brownian motion is barely seen because of the breakup with the connection with the convergence of Weierstrass function. The right subfigure

corresponds to the power spectrum of $1/k$ (α=0). It is seen that fluctuation becomes finer as α decreases. **Figure 2** displays replicas of FBM corresponding to $1/k^2$ and $1/k^{1.02}$

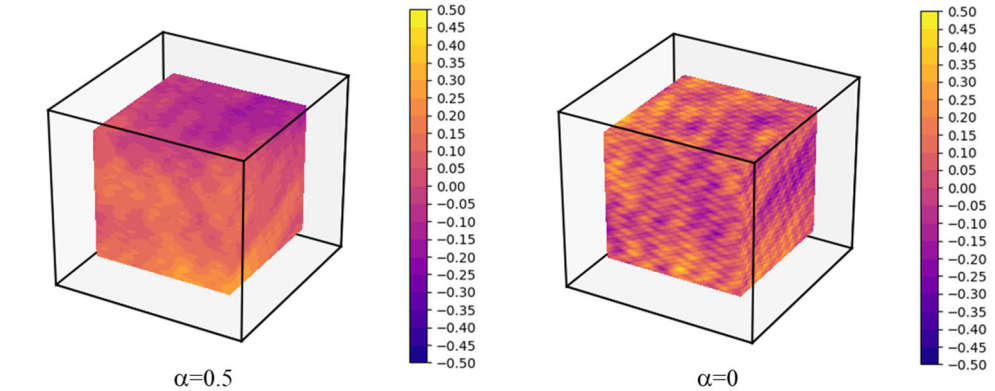

Figure 1. Plots of three-dimensional versions of IRWF corresponding to wave number range over [0.1, 100] ($m1$=-7, $m2$=16, λ=1.33352, S=50 cm, cubes: 100^3 cm^3 in 140^3 cm^3)

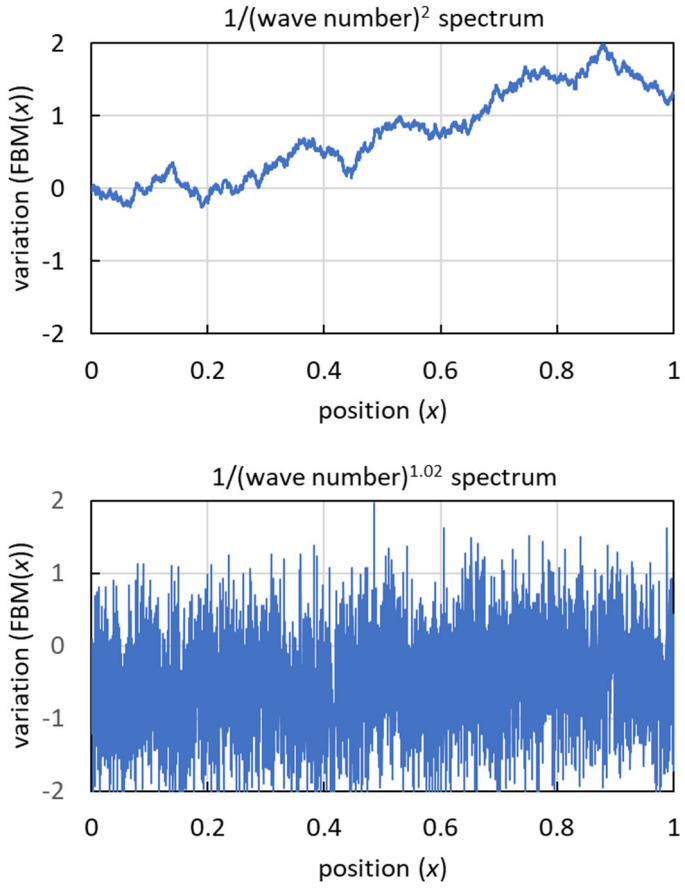

Figure 2. Plots of FBM corresponding to S=1 cm and wave number range (0, ∞)

spectra where the latter spectrum is chosen because FBM cannot represent the exact $1/k$ spectrum. It is seen that the deviation from zero mean can be persistent in the $1/k^2$ spectrum of FBM while the rapid and intense swinging around zero mean is characteristic of the $1/k^{1.02}$ spectrum. The three-dimensional transition between these two types of fluctuations corresponds to the change of colour texture in the subfigures of Figures 1.

For arbitrarily set lower and upper spectral ends k_1 (< 1) and k_2 (> 1), $W(x)$ in Eq (4) is rewritten as

$$\sigma\sum_{j=m1}^{0} B_j\lambda_1^{-\alpha j}\sin\left(\lambda_1^j x + A_j\right) + \sigma\sum_{j=1}^{\mathrm{m2}} B_j\lambda_2^{-\alpha j}\sin\left(\lambda_2^j x + A_j\right)$$

$$\lambda_1 > 1, \lambda_2 > 1, \alpha \geq 0, -\infty < m1 \leq 0 < m2 < \infty, \tag{27}$$

and the conditions $\lambda_1^{m1-1} = k_1$ and $\lambda_2^{m2} = k_2$ determine λ_1 and λ_2 once a choice is made for the numbers of terms $-m_1 + 1$ and m_2. In some cases, the power spectrum constructed from measurements is close to the white noise near zero frequency. In these cases, $Y(x)$ in Eq (16) and $W(x)$ in Eq (4) are combined as

$$\sigma\sum_{j=n1}^{\mathrm{n2}} B_{1j}\lambda_1^{(\alpha 1)j}\sin\left(\lambda_1^{-j} x + A_{1j}\right) + \sigma\sum_{j=m1}^{\mathrm{m2}} B_{2j}\lambda_2^{-(\alpha 2)j}\sin\left(\lambda_2^j x + A_{2j}\right),$$

$$\lambda_1 > 1, \lambda_2 > 1, \alpha 1 < 0, \alpha 2 \geq 0, -\infty < n1 \leq n2 < \infty, -\infty < m1 \leq m2 < \infty, \tag{28}$$

where B_{ij} and A_{ij} are, respectively, independent Bernoulli random variables taking ± 1 equally likely and independent random variables uniform on $[0, 2\pi)$. Since the spectral domain covered by the first and second sums are $[\lambda_1^{-n2}, \lambda_1^{-(n1-1)}]$ and $[\lambda_2^{m1-1}, \lambda_2^{m2}]$, respectively, a desired power spectrum will be obtained under the restriction $\lambda_1^{-(n1-1)} = \lambda_2^{m1-1}$ at the breakpoint frequency (<1). Each sum in Eqs (27) and (28) are then made three-dimensional as in Eqs (21) and (22).

3. Demonstration of IRWF

3.1 Description of sample problem

A sample problem to which IRWF is applied consists of the mixture of three boiling water reactor (BWR) fuels with different burnups placed in a sufficiently water-moderated environment. The material composition data are shown in **Table 1** and **2**. These data were computed using the SWAT 4.0 code system (Kashima et al, 2014). The geometry is shown in **Figure 3** where the inner sphere is occupied by BWR fuels in Table 1 and water in Table 2.

Table 1. BWR fuel composition data（unit: atoms/b cm）

	burnup (GWd/t)*		
	15.2	24..2	37.5
^{234}U	5.9808E-06	5.3923E-06	4.6383E-06
^{235}U	6.0824E-04	4.5413E-04	2.7596E-04
^{238}U	2.2847E-02	2.2889E-02	2.2926E-02
^{238}Pu	5.2710E-07	1.6461E-06	4.7983E-06
^{239}Pu	1.0731E-04	1.2499E-04	1.3421E-04
^{240}Pu	2.1475E-05	3.7581E-05	5.8905E-05
^{241}Pu	7.9357E-06	1.5211E-05	2.4107E-05
^{242}Pu	1.2858E-06	4.2769E-06	1.1965E-05
^{241}Am	2.3857E-06	4.7629E-06	7.8171E-06
^{95}Mo	2.2875E-05	3.5524E-05	5.2984E-05
^{99}Tc	2.3159E-05	3.6008E-05	5.4041E-05
^{103}Rh	1.3170E-05	2.0451E-05	2.9812E-05
^{143}Nd	1.9107E-05	2.8023E-05	3.7735E-05
^{145}Nd	1.3677E-05	2.1010E-05	3.0779E-05
^{147}Sm	5.2342E-06	7.6397E-06	1.0252E-05
^{149}Sm	1.1941E-07	1.1249E-07	1.0720E-07
^{150}Sm	4.4851E-06	7.5358E-06	1.2122E-05
^{152}Sm	2.0905E-06	3.1753E-06	4.3827E-06
^{153}Eu	1.4220E-06	2.7342E-06	4.8356E-06
^{155}Gd	2.7162E-07	1.2875E-07	2.0688E-07
^{157}Gd	4.5914E-08	4.4543E-08	4.3721E-08
O	4.8104E-02	4.8497E-02	4.9080E-02

* burnup under 70% void fraction and then 5 years of cooling

Table 2　Water（25℃）composition data（unit: atoms/b cm）

H	6.666E-02	O	3.333E-02

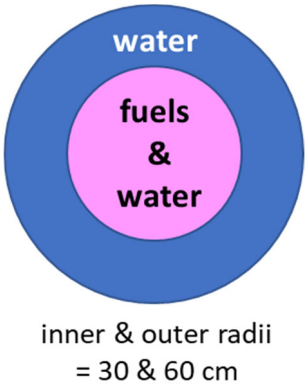

Figure 3. Spherical system of fuel mixture

Let BWR fuels in Table 1 be type 1, 2 and 3, respectively, according to 15.2 GWd/t, 24.2 GWd/t and 37.5 GWd/t. The macroscopic cross section Σ of the random mixture of these fuels is

$$\hat{\Sigma}_R(\mathbf{r}, E) = \hat{V}_1(\mathbf{r})\Sigma_{R,1}(E) + \hat{V}_2(\mathbf{r})\Sigma_{R,2}(E) + \hat{V}_3(\mathbf{r})\Sigma_{R,3}(E) \tag{29}$$

where the hat ^ indicates a replica, E is energy, R implies a nuclear reaction type, and $\hat{V}_i(\mathbf{r})$ $(i = 1,2,3)$ stand for space-dependent volume fractions. Obviously,

$$\hat{V}_1(\mathbf{r}) + \hat{V}_2(\mathbf{r}) + \hat{V}_3(\mathbf{r}) = 1, 0 \le \hat{V}_i(\mathbf{r}) \le 1, i = 1,2,3. \tag{30}$$

The mean volume fractions over replicas are assumed to be position-independent and separated into two nonnegative parts

$$\begin{aligned} V_1 &= E[\hat{V}_1(\mathbf{r})] = V_{1,2} + V_{1,3} \\ V_2 &= E[\hat{V}_2(\mathbf{r})] = V_{2,3} + V_{2,1} \\ V_3 &= E[\hat{V}_3(\mathbf{r})] = V_{3,1} + V_{3,2} \end{aligned} \tag{31}$$

where by Eq (30)

$$V_1 + V_2 + V_3 = 1. \tag{32}$$

The method of PVP (Ueki, 2021) determines the quantities on the righthand sides in Eq (31) by

$$V_{1,2}:V_{1,3} = V_2:V_3,\ V_{2,3}:V_{2,1} = V_3:V_1,\ V_{3,1}:V_{3,2} = V_1:V_2. \tag{33}$$

Denoting IRWF in Eq (21) as $W_{i,j}(\mathbf{r})$ for the BWR fuel pairing of types *i* and *j* and taking into account Eq (5), PVP computes the volume fractions in Eq (29) as

$$\hat{V}_1(\mathbf{r}) = V_{1,2} + V_{1,3} + min\left(V_{1,2}, V_{2,1}\right)\ W_{1,2}(\mathbf{r}) - min\left(V_{1,3}, V_{3,1}\right) W_{3,1}(\mathbf{r}),$$

$$\hat{V}_2(\mathbf{r}) = V_{2,3} + V_{2,1} + min\left(V_{2,3}, V_{3,2}\right)\ W_{2,3,}(\mathbf{r}) - min\left(V_{2,1}, V_{1,2}\right)\ W_{1,2}(\mathbf{r}),$$

$$\hat{V}_3(\mathbf{r}) = V_{3,1} + V_{3,2} + min\left(V_{3,1}, V_{1,3}\right)\ W_{3,1}(\mathbf{r}) - min\left(V_{3,2}, V_{2,3}\right)\ W_{2,3}(\mathbf{r}). \quad (34)$$

where $W_{i,j}(\mathbf{r})$ are independent of each other and can be replaced by $Y_{i,j}(\mathrm{r})$, i.e., IRWF in Eq (22). When the water-to-fuel volume ratio is $A_{H_2O}{:}\,A_{Fuel}$, the macroscopic cross section inside the inner sphere in Figure 4 is

$$\frac{A_{H_2O}}{A_{H_2O}+A_{Fuel}}\ \Sigma_R^{H_2O}(E) + \frac{A_{Fuel}}{A_{H_2O}+A_{Fuel}}\widehat{\Sigma}_R(\mathbf{r}, E). \quad (35)$$

where $\Sigma_R^{H_2O}(E)$ is the macroscopic reaction-type R cross section of water. Various parameters are set as $V_1 = 4/9$, $V_2 = 2/9$, $V_3 = 1/3$ and $A_{H_2O}{:}\,A_{Fuel} = 5{:}\,2$. These parameters and the geometry in Figure 3 are chosen so that essential features of fuel debris in a sufficiently water-moderated environment can be extracted. A series of Monte Carlo criticality calculations are carried out by Solomon (Nagaya et al, 2019) where the delta-tracking scheme by Spanier (Spanier, 1966) is available for the neutron transport computation under continuously varying macroscopic cross sections (Ueki, 2021). The JENDL 4.0 nuclear data libraries (Shibata et al, 2011) are used. The scaling factor *S* is set to 30 cm, the radius of the fuel and water region in Figure 3. The constant for amplitude adjustment σ is determined by the equality in Eqs (24)-(26). Each Monte Carlo criticality calculation corresponds to a replica of the triple $(F_{1,2}(\mathbf{r}), F_{2,3}(\mathbf{r}), F_{3,1}(\mathbf{r}))$, $F = W, Y$ and consists of 50000 neutrons per generation and 5200 generations with initial 200

generations discarded. This computational condition yields a k_{eff} standard deviation of 0.00006~0.00007 for each replica, i.e., a sufficiently small statistical error which allows one to evaluate the variation of k_{eff} over replicas of order $0.1\%\Delta k_{eff}/k_{eff}$ or larger.

3.2 Numerical results

Figure 4 shows the effect of spectral range on k_{eff} uncertainty evaluated over 100 replicas of the random media represented by Eq (35) under the $1/k^2$ power spectrum ($\alpha = 0.5$). Here, a visually displayed variation in k_{eff} is interpreted as the k_{eff} uncertainty due to the indeterminacy of the mixture formation of three fuels. It is clearly seen that low frequency domains are more influential on the fluctuation of k_{eff} than high frequency domains. This result is deemed conclusive since σ is determined in a fair manner by the equality in Eq (24) with $m2$=0, $m1$=-23, $\lambda = 1.33352$ for the left subfigure and $m2$=24, $m1$=1, $\lambda = 1.33352$ for the right subfigure. No error bar is shown for all replicas because the error bar of Monte Carlo criticality calculation on a single replica is smaller than the corresponding marker size.

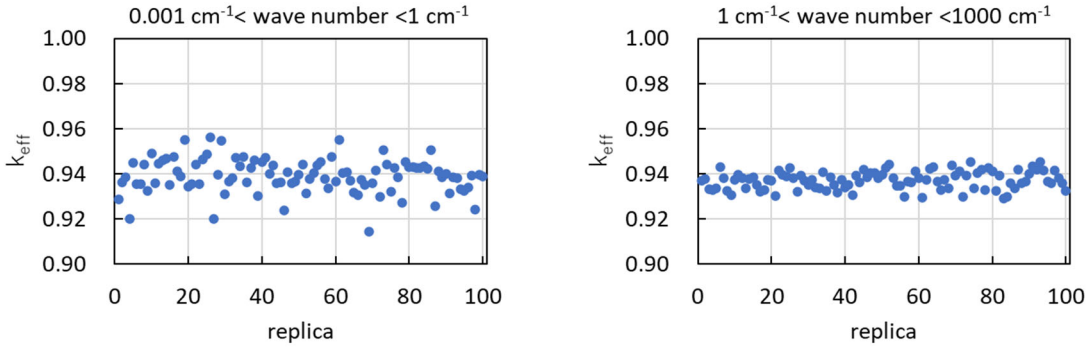

Figure 4. Effect of spectral range on k_{eff} uncertainty (1/(wave number)^2 spectrum case)

Figure 5 shows the effect of inverse power law on k_{eff} uncertainty evaluated over 100 replicas of the random media represented by Eq (35). The value of α ranges over -0.5, -0.25, -0.125, -0.01, 0.01, 0.125, 0.25, and 0.5, respectively, for the power spectra $1/k^0$

(white), $1/k^{0.5}$, $1/k^{0.75}$, $1/k^{0.98}$, $1/k^{1.02}$, $1/k^{1.25}$, $1/k^{1.5}$, $1/k^{2}$ (brown), and the spectral range is $0.1\ \text{cm}^{-1} \le k \le 100\ \text{cm}^{-1}$ by $m2$=16, $m1$=-7, $\lambda = 1.33352$ for $\alpha \ge 0$ and by $m2$=8, $m1$=-15, $\lambda = 1.33352$ for $\alpha < 0$. It is seen that k_{eff} uncertainty significantly decreases as the law of power spectrum approaches the white noise and the decreasing trend is nearly monotonic. This result is also deemed conclusive because the spectral range is fixed and σ is determined in a fair manner by the equalities in Eqs (24)-(26).

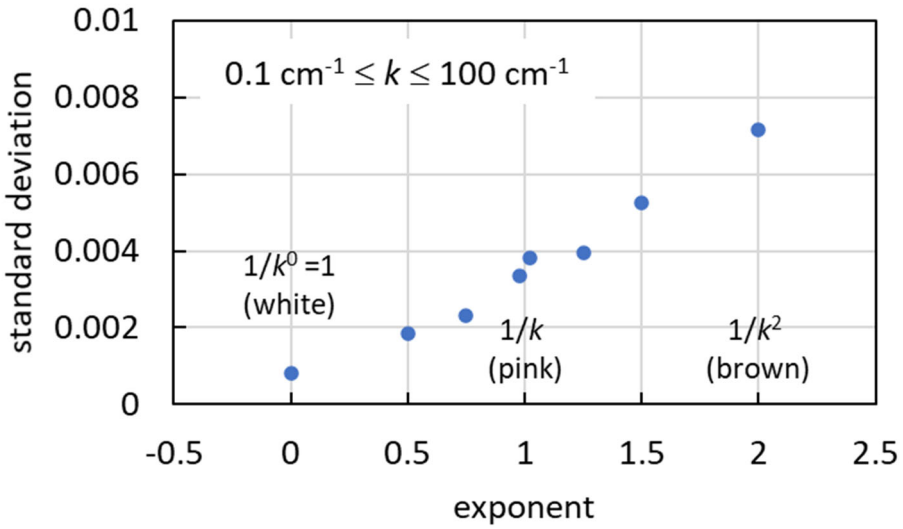

Figure 5. Effect of inverse power law on k_{eff} uncertainty over 100 replicas (k: wave number)

Figure 6 shows the effect of spectral range and inverse power law on k_{eff} uncertainty evaluated over 100 replicas of the random media represented by Eq (35). The parameters ($m1$, $m2$) for the four spectral ranges 0.001 $cm^{-1} \le k \le 1$ cm^{-1}, 0.01 $cm^{-1} \le k \le 10$ cm^{-1}, 0.1 $cm^{-1} \le k \le 100$ cm^{-1}, and 1 $cm^{-1} \le k \le 1000$ are, respectively, (1,24), (-7,16), (-15,8) and (-23,0) for the $1/k^0$ spectrum and (-23,0), (-15,8), (-7,16) and (1,24) for the $1/k^2$ spectrum. It is seen that the k_{eff} uncertainty of the $1/k^2$ spectrum stays relatively large as far as the spectral range includes $k < 1$ cm^{-1} while the k_{eff} uncertainty of the $1/k^0$ spectrum is small as far as the spectral range includes $k > 1$ cm^{-1}.

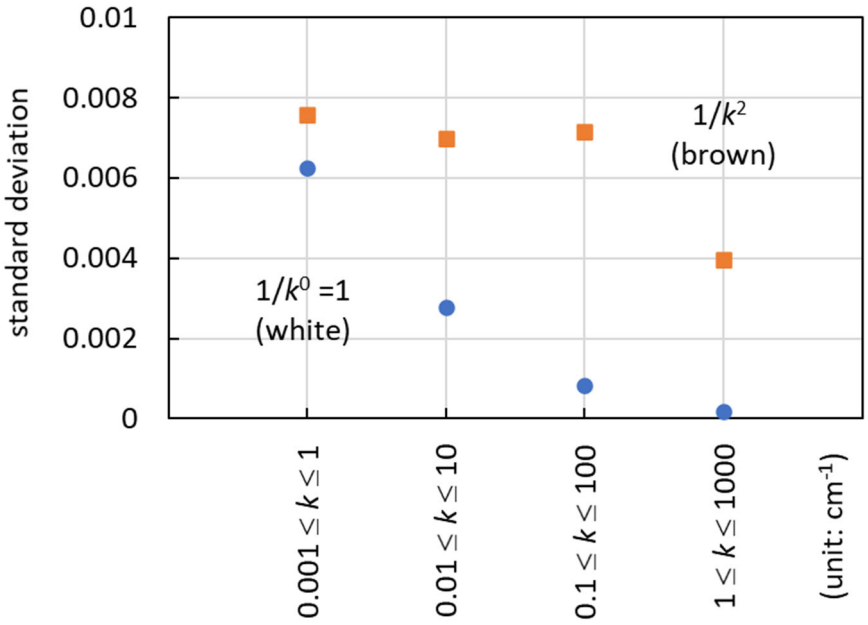

Figure 6. Effect of spectral range and inverse power law on k_{eff} uncertainty over 100 replicas (k: wave number)

All the results in Figures 4-6 cannot be obtained by RWF in previous works (Ueki, 2017; Ueki, 2021; Araki et al, 2021) because of the lack of the control capability of spectral range. Moreover, since the parameter $m1$ is always set to 1 in RWF, the comparison of the $1/k^0$ and $1/k^2$ spectra by RWF ends up with the one like comparing the $1/k^2$ spectrum over 1 $cm^{-1} \le k \le 1000$ cm^{-1} with the $1/k^0$ spectrum over 0.001 $cm^{-1} \le k \le$

$1cm^{-1}$. A judgment based on such a comparison is off the point in terms of Figure 6. On the other hands, the control capability of spectral range in IRWF can produce results like Figures 4-6 which will be valuable from an engineering judgment point of view. This is the most important achievement by IRWF.

4. Conclusions

In this work, Weierstrass function methodology which is termed IRWF has been established as a refined version of RWF. The main accomplishment of IRWF is the capability of discretely representing any inverse power law power spectrum between the arbitrarily set lower and upper ends of spectral range. The representation points are spaced at powers of a real number larger than unity. IRWF is thus suitable for realizing power spectrum in a desired domain over several orders of magnitude. Practically, IRWF gives reactor physicists an option of carrying out the uncertainty analysis of random media criticality under various inverse power law power spectra in terms of the identical spectral range and representation points. This enables reactor physicists to make fair criticality comparison for various random media. IRWF is demonstrated for the fluctuation of fuel debris criticality in a sufficiently water-moderated environment. The numerical results show that the frequency domains at small orders of magnitude are more influential on the fluctuation of k_{eff} than those at large orders of magnitude. All the new developments have been implemented in Solomon (Nagaya et al, 2019). Here, it is worthwhile pointing out that the implementation of IRWF in any Monte Carlo criticality and reactor physics code needs the delta-tracking method of neutron transport (Spanier and Gelbard, 1969) in order to handle macroscopic cross sections continuously varying in space.

The application of IRWF is fundamentally limited to the random media under power law power spectrum, i.e., a linear law on the logarithmic scale. However, in other cases, the uncertainty analysis of random media criticality may also be desired in terms of the

power spectrum under a different law represented on a linear scale. For example, a partially and insufficiently functioning cooling system may prevent extreme physical disorder from fully evolving into the state characterized by the inverse power law power spectrum. To cope with these realities, it will be necessary to develop a randomized function which can realize a power spectrum of arbitrary shape. It will also be of practical significance to introduce the method of overlaying voxels and unstructured meshes on random media in order to handle the precipitation of foreign substance. These challenges are avenues for new development in the foreseeable future.

Acknowledgment

The material composition data of BWR fuels in Section 3 were computed by Mr. T. Watanabe for a contract research (Criticality Safety Research Group, 2019) with Nuclear Regulation Authority (NRA) of Japan. Work reported in this paper was performed under the auspices of Secretariat of NRA.

References

Araki S, Yamane Y, Ueki T, Tonoike K., 2021. Effect of moderation condition on neutron multiplication factor distribution in$1/f^{\beta}$ random media. Nuclear Science and engineering. https://doi.org/10.1080/00295639.2021.1897732.

Bak P, Tang C, Wiesenfeld K., 1987. Self-Organized Criticality: An Explanation of 1/f Noise. Physical Review Letters. 1987; 59, 4, 381-384. https://doi.org/10.1103/PhysRevLett.59.381

Criticality Safety Research Group 2019, Japan Atomic Energy Agency. Development of Criticality Evaluation Method for Fuel Debris at TEPCO Fukushima Daiichi Nuclear Power Station – Fiscal Year 2018 Nuclear Regulation Authority

Commissioned Results Report: Minato-ku, Tokyo-to (Japan): Nuclear Regulation Authority, Japan; 2019. (https://iss.ndl.go.jp/books/R100000002-I030581534-00)

Dalziel SB, Linden PF, Youngs DL., 1999 Self-Similarity and Internal Structure of Turbulence Induced by Rayleigh-Taylor Instability. Journal of Fluid Mechanics. 1999; 339, 1-48. https://doi.org/10.1017/S002211209900614X

Falconer K., 2003. Fractal Geometry 2nd Ed. West Sussex, England (UK): John Wiley & Sons; 2003.

Frieden BR, Hughes RJ., 1994. Spectral 1/f Noise Derived from Extremized Physical Information. Physical Review E. 1994; 49**,** 4, 2644-2649. https://doi.org/10.1103/PhysRevE.49.2644

Kashima T, Suyama K, Takada T., 2014. SWAT4.0; The Integrated burnup code system driving continuous energy Monte Carlo codes MVP, MCNP and deterministic calculation code SRAC. Tokai-mura, Ibaraki-ken (Japan): Japan Atomic Energy Agency; 2014 (JAEA-Data/Code 2014-028).

Larmier C, Zoia A, Malvagi F, Dumonteil E, Mazzolo A., 2018. Neutron Multiplication in Random Media: Reactivity and Kinetics Parameters. Annals of Nuclear Energy. 2018; 111, 391-406. https://doi.org/10.1016/j.anucene.2017.09.006

Marinosci A, Larmier C, Zoia A., 2018. Neutron Transport in Anisotropic Random Media. Annals of Nuclear Energy. 2018; 118, 406-413. https://doi.org/10.1016/j.anucene.2018.04.031

Miller SL, Miller WM, McWhorter PJ., 1993. Extremal Dynamics: A Unifying Physical Explanation of fractals, 1/f Noise, and Activated Processes. Journal of Applied Physics. 1993; 73, 6, 2617-2628. https://doi.org/10.1063/1.353079

Nagaya Y., Ueki T., Tonoike K., 2019. SOLOMON: A Monte Carlo Solver for Criticality Safety Analysis," *Proceedings of ICNC 2019*, Paris, France, September 15-20, 2019.

Reed IS, Lee PC, Truong TK., 1995 Spectral Representation of Fractional Brownian Motion in n Dimensions and its Properties. IEEE Transactions on Information Theory. 1995; 41, 5, 1439-1451. DOI: 10.1109/18.412687

Shibata K et al., 2011. JENDL 4.0: A New Library for Nuclear Science and Engineering. Journal of Nuclear Science and Technology. 2011; 48, 1, 1-30. https://doi.org/10.1080/18811248.2011.9711675

Spanier J., 1966. Two Pairs of Families of Estimators for Transport Problems. SIAM Journal on Applied Mathematics. 1966; 14(4), 702-713. https://doi.org/10.1137/0114059

Spanier J, Gelbard EM, 1969. Monte Carlo Principles and Neutron Transport Problems. Addison-Wesley Publishing Company; reprinted from Dover Publications, Mineola, N.Y. U.S.A; 2008.

Tatsumi T., 1982. Fluid Mechanics. Chiyoda-Ku Tokyo (Japan); Bai-Fu-Kan; 1982.

Ueki T., 2017. Monte Carlo Criticality Analysis under Material Distribution Uncertainty. Journal of Nuclear Science and Technology. 2017; 54, 3, 267-279. https://doi.org/10.1080/00223131.2016.1260066

Ueki T., 2021. Monte Carlo Criticality Calculation of Random Media Formed by Multimaterials Mixture Under Extreme Disorder. Nuclear Science and Engineering. 2021;195, 214-226. https://doi.org/10.1080/00295639.2020.1801000